Title: Extreme Oxidant Amounts Produced by Lightning in Storm Clouds

One Sentence Summary: Lightning-generated hydroxyl radicals can provide a significant fraction of total global atmospheric oxidation.

Authors: W. H. Brune[1*], P. J. McFarland[1], E. Bruning[2], S. Waugh[3], D. MacGorman[3], D. O. Miller[1], J. M. Jenkins[1], X. Ren[4,5], J. Mao[6], J. Peischl[7,8]

Affiliations:

[1] Department of Meteorology and Atmospheric Science, Pennsylvania State University, University Park, PA

[2] Department of Geosciences, Texas Tech University, Lubbock, TX

[3] National Severe Storms Laboratory, National Oceanic and Atmospheric Administration, Norman, OK

[4] Department of Atmospheric and Oceanic Science, University of Maryland, College Park, MD

[5] Air Resources Laboratory, National Oceanic and Atmospheric Administration, College Park, MD

[6] Department of Chemistry and Biochemistry, University of Alaska, Fairbanks, Fairbanks, AK

[7] Cooperative Institute for Research in Environmental Sciences, University of Colorado, Boulder, CO

[8] NOAA Chemical Sciences Laboratory, Boulder, CO

*Corresponding author: Email: whb2@psu.edu

Abstract: Lightning increases the atmosphere's ability to cleanse itself by producing nitric oxide (NO), leading to atmospheric chemistry that forms ozone (O_3) and the atmosphere's primary oxidant, the hydroxyl radical (OH). Our analysis of a 2012 airborne study of deep convection and chemistry demonstrates that lightning also directly generates the oxidants OH and the hydroperoxyl radical (HO_2). Extreme amounts of OH and HO_2 were discovered and linked to visible flashes occurring in front of the aircraft and to subvisible discharges in electrified anvil regions. This enhanced OH and HO_2 is orders of magnitude more than any previous atmospheric observation. Lightning-generated OH in all storms happening at the same time globally can be responsible for a highly uncertain but substantial 2-16% of global atmospheric OH oxidation.

Lightning contributes to the atmosphere's ability to cleanse itself through the production of reactive nitric oxide (NO) followed by its subsequent chemistry. The atmosphere's two primary oxidants, the hydroxyl radical (OH) and ozone (O_3), are produced when the lightning NO reacts with the hydroperoxyl radical (HO_2) to produce OH and nitrogen dioxide (NO_2). NO_2 then decomposes in sunlight, leading to O_3 formation. The direct generation of O_3 from lightning (LO_3) has been inferred but not unambiguously observed in the atmosphere (*1-3*). Lightning production of nitrogen oxides (LNO_x) was first suggested in the early nineteenth century (*4*) and, in the past four decades, has been studied intensively in the atmosphere, laboratory, and model simulation (*5-18*). When global models of atmospheric chemistry include parameterized LNO_x emissions, tropospheric NO_x, O_3, and OH all increase substantially, primarily in the tropical to subtropical upper troposphere (*19*).

Electrified storms have charge distributions that are more horizontally stratified in anvils than in storm cores, but both anvils and cores contain granular electric field and charge distributions

(*20,21*), resulting in a range of electrical currents, from subvisible discharges to visible flashes (*22-25*). Some subvisible discharges have sufficient energy to overcome the dissociation bond strengths of H_2O, producing OH, H, and HO_2, and of O_2, producing O_3. Only visible flashes have sufficient energy also to dissociate N_2, which has a bond dissociation energy almost twice that of H_2O and O_2, and to initiate the high-temperature chemistry that leads to NO formation (*26*). Previous modeling studies of lightning flash chemistry calculated that large amounts of OH and HO_2 ($OH+HO_2=HO_x$) are produced by visible flashes, but the calculated OH lifetime is only milliseconds, too short for lightning HO_x (LHO_x) to contribute noticeably to atmospheric oxidation (*27,28*).

However, these studies did not consider OH exposure, which is the integral of the OH concentration multiplied by time (Eq. 1).

$$OH_{exposure} = \int [OH]\, dt \quad (1)$$

OH exposure multiplied by the reaction rate coefficient between OH and another trace gas determines how much of that gas will be destroyed. If each of the lightning flashes and subvisible electrical discharges occurring simultaneously around the globe produces large amounts of OH and HO_2, it is possible that, even for short exposure times, LHO_x could make substantial contributions to the atmosphere's total OH exposure and therefore its oxidative capacity.

The NASA DC-8 aircraft flew through anvils of deep convective clouds during the Deep Convective Clouds and Chemistry (DC3) field study in summer 2012 (*29*). The aircraft carried instruments to measure in situ almost 100 atmospheric constituents, including OH and HO_2, which were measured by the Airborne Tropospheric Hydrogen Oxides Sensor (ATHOS, see

Supplement). Typically, the DC-8 flew in the near-surface inflow region of a growing convective cell, spiraled up outside of it, and then sampled the convection outflow anvil. Simultaneously, a lightning mapping array (LMA) on the ground measured the position and intensity of the flashes within the convective storm and its anvil. Thus, DC3 presented an excellent opportunity to discover whether subvisible discharges and visible flashes produce substantial amounts of LHO_x.

Results from the 22-23 June flight

The DC-8 spent the most time in an anvil of active deep convection on 22-23 June over Colorado (**Fig. 1**). The DC-8 executed a low pass at 40.8° N latitude (**Fig. 1 A**) before spiraling up beside the growing convective storm to 10 km altitude. HO_x was 5-20 pptv outside of the anvil, typical amounts for these altitudes (*30*). The first instance of enhanced HO_x of ~700 pptv was measured in the cloud on the edge of the storm convective core at 7 km altitude during the spiral, but all the other enhanced HO_x was observed as the DC-8 passed back and forth through the electrified anvil at three different altitudes between 10 and 11 km (**Fig. 1 A and B**). Finally (**Fig. 1 C**), after the DC-8 did a loop through a fire plume (**Fig. 1 C**, upper left), it passed through the edge of another convective cell to the south, where enhanced HO_x was observed again. These coincidences between enhanced HO_x and electrified regions in the convection anvils indicate that electrical discharges were the source of enhanced OH and HO_2.

A time series of measured HO_x, NO_x, and O_3 shows that HO_x and NO_x were enhanced only within the convection anvil, which is indicated by the ice water content (IWC) (**Fig. 2**). The HO_x and NO_x enhancements varied substantially in terms of peak values and duration, with enhanced HO_x varying from tens to thousands of pptv and persisting for distances between 0.1 to 8 km along the flight track. OH was often about half of enhanced HO_x (**Fig. 2**, insert).

Prior to this flight, the most HO_x ever observed in the atmosphere was about 150 pptv for HO_2 and a few pptv for OH (*24*,*25*). Thus, these discharge-generated OH and HO_2 amounts are orders of magnitude above any amounts ever seen before in the atmosphere.

The NO_x enhancements above background were a few ppbv to occasionally more than 10 ppbv, as has been seen before (*14*,*16*,*17*). The enhanced HO_x and enhanced NO_x sometimes coincided, but not always, for two reasons. First, the NO_x lifetime is at least several hours, while the HO_x lifetime is at most a few minutes. Thus, enhanced NO_x could have come from Earth's boundary layer or from visible flashes in the convection core or anvil several minutes before the DC-8 arrived, while any lightning-generated enhanced HO_x would have reacted away. Second, enhanced HO_x with little to no enhanced NO_x is generated by weak subvisible electrical discharges because H_2O and O_2 have about half the bond dissociation energies of N_2 and NO production requires high-temperature chemistry (*26*).

About one-third of the time, HO_x was enhanced in anvil regions where no electrical activity was detected by the LMA (**Fig. 2**, inset). For instance, the enhanced HO_x on the right of the inset reaches 700 pptv while NO_x and O_3 were only a few times background, all in the anvil but outside of regions in which the LMA detected flashes. Thus, enhanced HO_x appears to be generated even by subvisible discharges too weak for the LMA to detect (*32*).

Some HO_x enhancements were accompanied by O_3 enhancements (**Fig. 2**). On the other hand, the DC-8 encountered stratospheric-like air that had wrapped itself around the outside of the anvil (*33*) and O_3 at the edge of the anvil often suddenly increased by as much as 100 ppbv, such as at 00:32 in **Fig 2**. Thus, it is difficult to say with certainty that these coincident O_3

enhancements were definitely produced by electrical discharges, even though our laboratory studies show that they can be (*26*).

A careful review of the NASA DC-8 forward camera revealed several sub-second instances of visible lightning, including one at 00:16:01 and another at 00:16:11 UTC on 23 June. Less than a second after each visible lightning flash, large sub-second HO_x enhancements were measured. Enhancements may also have been seen in NO_x and O_3, but they are thought not to be credible and were not included in the data set (see Supplement for explanation). Both flashes occurred in front of the aircraft and were recorded by the aircraft forward camera as short white lines that lasted just one frame (<33 ms). The second flash is seen as the short, curved white line in the photograph in **Fig. 3** and is just a small segment of a much larger flash, according to the LMA (**Fig. S1**). A few tenths of a second later, observed HO_x was enhanced by 2000 pptv (**Fig. 3**, insert). The time delay between the flash in the video and the enhanced HO_x indicates that this flash segment occurred tens of meters in front of the aircraft traveling at 200 m s^{-1}. This result is consistent with the timing between the LMA flash and the enhanced HO_x spike in **Fig. S1**. Note that, for the smaller more diffuse HO_x spikes preceding and following these two flashes, no flashes were seen by either the forward or nadir camera. Because in-flight and laboratory evidence demonstrates that these HO_x spikes were generated by atmospheric electrical discharges (see Supplementary Material and **Fig. S2.**), these observations provide conclusive evidence that lightning produces extreme amounts of HO_x.

Modeling the evolution of HO_x and NO_x

Several observations of enhanced HO_x peaks were modeled with a photochemical box model that was constrained with other DC-8 measurements (*30*). Of these, two cases are shown in **Fig. 3.**

For the first case at 00:09:37, no visible flash was observed and the model was initialized with 0.5 ppbv of NO_x, 70 ppbv of O_3, and 700 pptv of HO_x. For the second case at 00:16:11, the DC-8 sampled the air affected by the visible flash in **Fig. 3** and the model was initialized with 230 ppbv of NO_x and 400 ppbv of O_3, which were estimated from laboratory measurements, and 2000 pptv of HO_x. The names and numerical values for the other most important constraining chemical species is provided in the Photochemical Box Modeling section of the Supplemental Material.

Calculated OH and HO_2 decay to background levels within a few minutes for the subvisible discharge case and within a second for the visible flash case. NO_x is effectively constant because its lifetime is typically several hours (*18*), although NO reacts with O_3 to produce NO_2. For the low-NO_x case (a), the calculated OH and HO_2 decays are due primarily to the reactions $OH + HO_2 \rightarrow H_2O + O_2$ with a small contribution from $OH + NO + M \rightarrow HONO + M$, but for the high-$NO_x$ case (b), the OH and HO_2 decays are due primarily to the reactions $OH + NO + M \rightarrow HONO + M$ and $OH + NO_2 + M \rightarrow HNO_3 + M$, with only a small contribution from $OH + HO_2 \rightarrow H_2O + O_2$.

As a result, the calculated OH exposure is 9.7×10^9 molecules cm^{-3} s for the case (a) and 1.2×10^9 molecules cm^{-3} s for case (b). Note that the OH exposure is the result of all OH production and loss processes. Once an electrical discharge produces enhanced OH and HO_2, then OH will decay in a predictable way based on the rates of OH production, predominantly HO_2 reactions with NO and O_3, and the rates of OH loss to HO_2, NO, NO_2, CO, CH_4, and all other OH reactants. The OH exposure is just the integral of this decaying OH concentration over time (Eq. 1). Thus, for example, if a flash occurs once a second in the same volume of air, then the OH

exposure (molecules cm^{-3} s) per flash times one flash per second will be the average OH concentration (molecules cm^{-3}) for that volume of air.

All flights into electrified anvils

Enhanced HO_x was observed on eight flights, always within electrified convective cores or anvils. On most flights, the DC-8 either flew inside the edge of the anvil or made only a few passes through it (**Figs. S3 and S4**). For Table 1, the OH exposure was calculated for nine HO_x enhancements chosen to represent a range of initial HO_x and NO_x values, with four from the 22-23 June flight (**Fig. 2**). HO_x was enhanced by hundreds to thousands of pptv on all these flights, generally with little or no enhanced NO_x and O_3 and infrequent visible lightning. Peak OH was 125 to 600 pptv. As a result, the OH exposure calculated for these other flights was $3.3\text{-}11.8 \times 10^9$ OH molecules cm^{-3} s, consistent with that from the peaks on 22-23 June. Thus, the results from 22-23 June appear to be typical of the other DC3 flights in electrified storm anvils over Colorado or Oklahoma.

The electric field vertical structure was measured with balloon-borne electrometers in convection also sampled by the DC-8 over Oklahoma on 19-20 May and 29 May (Fig. S3 and S4). These storms had negative electric field extrema of -20 and -80 kV m^{-1} and positive extrema of 10 to 40 kV m^{-1}, although the arrangement of negative and positive charge layers between these maxima was different between the two storms. These higher values are consistent with the breakdown electric fields that need to be exceeded before lightning can be initiated (*37*) and are fairly typical of the electric fields in electrified convection.

Discussion

Direct production of OH and HO_2 has now been observed in the anvils of deep convective clouds. The peak HO_x values were similar for subvisible discharges and the much less frequent visible flashes in regions where the LMA detected electrical discharges. In addition, about a third of enhanced HO_x was measured in the storm clouds outside of regions where the LMA detected flashes, indicating that low-energy subvisible electrical discharges not detected by the LMA also produced enhanced HO_x.

Global chemical transport models include parameterizations that use estimated LNO_x per visible flash (moles $flash^{-1}$ or molecules $flash^{-1}$) and thunderstorm visible flash distributions and then spread the LNO_x molecules throughout the grid cells affected by a visible flash to produce NO and NO_2 concentrations (*36*). Parameterizing LHO_x will be more complicated because so much of it comes from subvisible discharges. Our recent laboratory experiments have determined the LHO_x generated by individual sparks and subvisible discharges in terms of molecules m^{-1} $discharge^{-1}$ (*26*), but, in an electrified storm, LHO_x is likely generated by complex structures of subvisible discharges that vary in space and time but are currently unknown. At present, we can use only the OH mixing ratios measured during DC3 to estimate the LHO_x impact on atmospheric oxidation.

How important is LHO_x for atmospheric oxidation? For context, consider the global mean OH exposure per second, which is the same as the global mean number of OH molecules. Global model estimates of the mean [OH] are $1.03 – 1.15 \times 10^6$ cm^{-3} (*37-42*), with an estimated uncertainty of ~25%, 68% confidence. Here we use the global number of OH molecules calculated from a global chemistry-climate model, which is 4×10^{30} molecules (*42*).

Two methods for estimating the OH generated each second by LHO_x are described in the Supplementary Material. Both methods assume that the amount of enhanced HO_x observed along the DC-8 flight path through the anvil represents the amount of enhanced HO_x generated throughout the electrified anvil region. Both use the typical LMA volume (**Table S1**), the fraction of the flight track for which the electrical discharge occurred within the past second, and the typical OH exposure per electrical discharge. The first method uses flash rates and the second method uses the ratio of enhanced HO_x inside and outside of the regions in which the LMA detected electrical discharges but still inside the anvil. From these calculations, the convective cell anvil on 22 - 23 June generated $2.7x10^{26}$ molecules for each second by the first method and $3.1x10^{25}$ molecules for each second by the second method.

The global number of active convective cells for each moment is thought to be 1800 (*12)*. Thus, the electrically charged storm anvils generated $4.9x10^{29}$ molecules each second by the first method and $5.6x10^{28}$ by the second method. The numbers are similar for the convective cell anvil sampled on 29 May (**Table S2**). As a result, LHO_x in convective cell anvils could be responsible for 1.4 - 12% of global OH.

LHO_x contributes to the global OH in two other ways. First, much of the HONO produced from the reaction of enhanced OH and NO would eventually be exposed to sunlight, releasing OH and increasing the contribution of LHO_x to global OH even more. Second, from the DC3 LMA data, the convective core on 22-23 June had 70% of the flashes (**Fig. 1**). During the spiral up on both 29 May and 23 June, the DC-8 flew through clouds associated with the convective core, encountering almost continuous enhanced HO_x in those clouds even though the DC-8 was

kilometers from the nearest flashes. If total electrical activity is proportional to flash extent, then this core could have produced an OH exposure about a third that of the anvil, increasing the LHOx contribution to global OH to 2 - 16%.

We emphasize that these estimates of the LHOx contribution to global OH are highly uncertain by perhaps a factor of ten (**Fig. S5**). These storms, their electrical activity, or their LHO_x generation may be atypical of global storms because Colorado and Oklahoma storms have different lightning characteristics from the more numerous tropical and subtropical storms (*43*). In addition, LHO_x generation by subvisible discharges as well as visible flashes makes estimating LHO_x more uncertain than estimating LNO_x. Thus, the ratio of LHO_x to LNO_x varies from less than 0.01 for visible flashes to more than 1000 for subvisible discharges. None-the-less, it may be possible to relate LHO_x to LNO_x, but not from the DC3 data alone. These uncertainties must be narrowed before LHO_x can be included with any confidence in global chemical transport models and climate models.

Narrowing the LHO_x production uncertainty requires sampling a variety of electrified storms with an aircraft instrumented to measure environmental conditions, cloud particle properties, water vapor, electric fields and charge distributions, electrical discharge video and sound, OH, HO_2, NO, NO_2, O_3, and HONO at 5 Hz or faster. At a minimum, this aircraft should sample electrified anvils at different distances from the core, but optimally, it should penetrate the core itself at different altitudes. These storms should be observed simultaneously by an LMA and satellites. Such aircraft studies would determine the globally observed factors needed to parameterize LHO_x in models.

LHO_x is contributing to the global OH calculated from observations of atmospheric constituents that react with OH, such as methane or methyl chloroform (*37-42*), implying that the OH actually produced by standard atmospheric chemistry is less than currently calculated. In addition, the impact of LHO_x on different atmospheric constituents depends on where it is generated. Our laboratory studies (*26*) indicate that LHO_x is generated in storm cores, cloud-to-ground lightning, and possibly even near high-voltage power lines, as well as in storm cloud anvils. Thus, LHO_x could be contributing to regional and global oxidation well beyond the storm cloud anvils. Furthermore, LHO_x may well be a larger contributor to global atmospheric oxidation than LNO_x. It is reasonable to assume that, in a warmer climate, an increase in storm intensity and lightning will increase the importance of lightning-generated OH to regional and global atmospheric oxidation.

References and Notes:

1. R.E. Orville, Ozone production during thunderstorms, measured by the absorption of ultraviolet radiation from lightning. *J. Geophys. Res*. **72**, 14, 3557-3561 (1967).
2. H. Bozem *et al.*, Influence of corona discharge on the ozone budget in the tropical free troposphere: a case study of deep convection during GABRIEL. *Atmospheric Chemistry and Physics* **14**, 8917-8931, https://doi:10.5194/acp-14-8917-2014, (2014).
3. H. Huntrieser *et al.*, On the origin of pronounced O_3 gradients in the thunderstorm outflow region during DC3. *J. Geophys. Res. Atmos.* **121**, 6600-6637 (2016).
4. J. von Liebig, Note sur la Nitrification. *Ann. Chem. Phys.* **35**, 329–333 (1827).

5. A.F. Tuck Production of nitrogen oxides by lightning discharges. *Q. J. Roy. Meteor. Soc.* **102**, 749-755, https://doi.org/10.1002/qj.49710243404 (1976).
6. W. L. Chameides, D. H. Stedman, R. R. Dickerson, D. W. Rusch, R. J. Cicerone, NO_x production in lightning. *J. Atmos. Sci.* **34**, 143-149 (1977).
7. E. Franzblau, C. J. Popp, Nitrogen oxides produced from lightning. *J. Geophys. Res.* **94(D8)**, 11089-11104 (1989).
8. C. Price, J. Penner, and M. Prather, NOx from lightning. 1. Global distribution based on lightning physics. *J. Geophys. Res.* **102**, 5929–5941, doi:10.1029/96JD03504 (1997).
9. Y. Wang, A. W. DeSilva, G. C. Goldenbaum, R. R. Dickerson, Nitric oxide production by simulated lightning: Dependence on current, energy, and pressure. *J. Geophys. Res.* **103(D15)**, 19149-19159, doi:10.1029/98JD01356 (1998).
10. A. J. DeCaria *et al.*, A cloud scale model study of lightning-generated NO_x in an individual thunderstorm during STERAO-A. *J. Geophys. Res.* **105(D9)**, 11601-11616 (2000).
11. B. Ridley *et al.*, Florida thunderstorms: A faucet of reactive nitrogen to the upper troposphere. *J. Geophys. Res.* **109**, doi:10.1029/2004JD004769 (2004).
12. A. J. DeCaria, K. E. Pickering, G. L. Stenchikov, L. E. Ott, Lightning-generated NO_x and its impact on tropospheric ozone production: A three-dimensional modeling study of a Stratosphere-Troposphere Experiment: Radiation, Aerosols and Ozone (STERAO-A) thunderstorm. *J. Geophys. Res.* **110**, D14303, doi:10.1029/2004JD005556 (2005).
13. B.A. Ridley *et al.*, Sampling of chemical constituents in electrified convective systems: Results and cautions. *J. Atmos. Chem.* **54,** 1–20, doi:10.1007/s10874-005-9007-5 (2006).

14. L. E. Ott *et al.*, Production of lightning NOx and its vertical distribution calculated from three-dimensional cloud-scale chemical transport model simulations. *J. Geophys. Res.* **115**, D04301, doi:10.1029/2009JD011880 (2010).

15. H. Huntrieser *et al.*, Injection of lightning-produced NO_x, water vapor, wildfire emissions, and stratospheric air to the UT/LS as observed from DC3 measurements. *J. Geophys. Res. Atmos*, **121**, 6638-6668 (2016).

16. U. Schumann, H. Huntrieser, The global lightning-induced nitrogen oxides source. *Atmos. Chem. Phys.* **7**, 3823-3907. https://doi.org/10.5194/acp-7-3823-2007 (2007).

17. I. B. Pollack *et al.*, Airborne quantification of upper tropospheric NO_x production from lightning in deep convective storms over the United States Great Plains. *J. Geophys. Res. Atmos.* **121**, 2002-2028 (2016).

18. B. A. Nault *et al.*, Lightning NO_x emissions: reconciling measured and modeled estimates with updated NO_x chemistry. *Geophys. Res. Lett.* **44**, 9479-9488 (2017).

19. L. J. Labrador, R. von Kuhlmann, M.G. Lawrence, The effects of lightning-produced NOx and its vertical distribution on atmospheric chemistry: Sensitivity simulations with MATCH-MPIC. *Atmos. Chem. Phys.* **5**, 1815–1834. https://doi.org/10.5194/acp-5-1815-2005 (2005).

20. J. E. Dye *et al.*, Electric fields, cloud microphysics, and reflectivity in anvils in Florida thunderstorms. *J. Geophys. Res.* **112**, D11215, doi:10.1029/2006JD007550 (2007).

21. S. A. Weiss, D. R. MacGorman, and K. M. Calhoun, Lightning in the anvils of supercell thunderstorms. *Mon. Wea. Rev.* **140**, 2064–2079, doi:10.1175/ MWR-D-11-00312.1 (2012).

22. D. Petersen, M. Bailey, W. H. Beasley, and J. Hallett, A brief review of the problem of lightning initiation and a hypothesis of initial lightning leader formation. *J. Geophys. Res. Atm.* **113** (D17), doi: 10.1029/2007JD009036 (2008).

23. D. Petersen, M. Bailey, J. Hallett, W. Beasley, Laboratory investigation of corona initiation by ice crystals and its importance to lightning. *Q. J. Roy. Meteor. Soc.* **141**, 1283–1293, doi:10.1002/qj.2436 (2014).

24. W. Rison *et al.*, Observations of narrow bipolar events reveal how lightning is initiated in thunderstorms. *Nat. Commun*. **7**, 1-11, DOI: 10.1038/ncomms10721 (2016).

25. A. Y. Kostinskiy, T. C. Marshall, M. Stolzenburg, The Mechanism of the Origin and Development of Lightning From Initiating Event to Initial Breakdown Pulses (v.2). *J. Geophys. Res. Atmos.* **125**, e2020JD033191, https://doi.org/10.1029/2020JD033191 (2020).

26. J. M. Jenkins, W. H. Brune, D. O. Miller, Lightning HO_x: Laboratory studies, *J. Geophys. Res. Atmos.*, (to be published simultaneously with this paper).

27. R.D. Hill, R. G. Rinker, Production of nitrate ions and other trace species by lightning. *J. Geophys. Res. Oc.* **86**, 3203-3209. https://doi.org/10.1029/JC086iC04p03203 (1981).

28. B. A. Bhetanabhotla, B. A., Crowell, A., Coucouvinos, R.D. Hill, R.G. Rinker, Simulation of trace species production by lightning and corona discharge in moist air. *Atmos. Environ.* **19**, 1391-1397, https://doi.org/10.1016/0004-6981(85)90276-8 (1985).

29. M. C. Barth *et al.*, The deep clouds and chemistry (DC3) field campaign. *Bull. Amer. Meteor. Soc.* **96**, 1281-1309 (2015).

30. W. H. Brune *et al.*, Atmospheric Oxidation in the presence of clouds during the Deep Convective Clouds and Chemistry (DC3) experiment. *Atmos. Chem. Phys.* **18**, 14493-14510 (2018).

31. D. Stone, L.K. Whalley, D.E. Heard, Tropospheric OH and HO_2 radicals: field measurements and model comparisons. *Chem. Soc. Rev.* **41**, 6348–6404 (2014).

32. V. C. Chmielewski, E. C. Bruning, Lightning Mapping Array flash detection performance with variable receiver thresholds. *J. Geophys. Res. Atmos.* **121**, 8600-8614 (2016).

33. L. L. Pan *et al.*, Thunderstorms enhance tropospheric ozone by wrapping and shedding stratospheric air. *Geophys. Res. Lett.* **41**, 7785–7790, doi:10.1002/2014GL061921 (2014).

34. R. J. Thomas *et al.*, Accuracy of the Lightning Mapping Array. *J. Geophys. Res.* **109**, D14207 (2004).

35. T. C. Marshall, M. P. McCarthy, W. D. Rust, Electric field magnitudes and lightning initiation in thunderstorms, *J. Geophys. Res.* **100**, 7097-7103 (1995).

36. L. T. Murray, D. J. Jacob, J. A. Logan, R. C. Hudman, W. J. Koshak, Optimized regional and interannual variability of lightning in a global chemical transport model constrained by LIS/OTD satellite data. *J. Geophys. Res.* **117**, D20307, doi:10.1029/2012JD017934 (2012).

37. R. Prinn *et al.*, Atmospheric trends and lifetime of CH_3CCl_3 and global OH concentrations. *Science* **269**, 187–192 (1995).

38. S. A. Montzka *et al.*, New Observational constraints for atmospheric hydroxyl on global and hemispheric scales, *Science* **288**, 500, doi:10.1126/science.288.5465.500 pmid:10775106, (2000).

39. M. G. Lawrence, P. J¨ockel1, and R. von Kuhlmann1, What does the global mean OH concentration tell us?. *Atmos. Chem. Phys.* **1**, 37-49, https://doi.org/10.5194/acp-1-37-2001, (2001)

40. J. Lelieveld, S. Gromov, A. Pozzer, and D. Taraborrelli, Global tropospheric hydroxyl distribution, budget and reactivity. *Atmos. Chem. Phys*. **16**, 12477–12493, (2016).

41. M. Li *et al.*, Tropospheric OH and stratospheric OH and Cl concentrations determined from CH_4, CH_3Cl, and SF_6 measurements. *npj Clim. Atmos. Sci.* **1**:29, doi:10.1038/s41612-018-0041-9, (2018).

42. A. T. Archibald *et al.*, Impacts of HO_x regeneration and recycling in the oxidation of isoprene: Consequences for the composition of past, present and future atmospheres. *Geophys. Res. Lett*. **38**, L05804, doi:10.1029/2010GL046520 (2011).

43. E. Williams, V. Mushtak, D. Rosenfeld, S. Goodman, D. Boccippio, Thermodynamic conditions favorable to superlative thunderstorm updraft, mixed phase microphysics and lightning flash rate. *Atmos. Res.* **76**, 288-306 (2005).

44. E. C. Bruning, Streamed clustering of lightning mapping data in Python using sklearn, presented at 12th Python in Science Conference (SciPy), Austin, TX, June 2013.

45. B. R. Fuchs *et al.*, Climatological analysis of LMA data with an open-source lightning flash-clustering algorithm. *J. Geophys. Res. Atmos*, **121**, 8625-8648 (2016).

46. B. M. Basarab, S. A. Rutledge, B. R. Fuchs, An improved lightning flash rate parameterization developed from Colorado DC3 thunderstorm data for use in cloud-resolving chemical transport models. *J. Geophys. Res. Atmos.* **120**, 9481-9499 (2015).

47. T. C. Davis, S. A. Rutledge, B. R. Fuchs, Lightning location, NO_x production, and transport by anomalous and normal polarity thunderstorms. *J. Geophys. Res. Atmos.* **124**, 8722-8742 (2019).

48. S. A. Weiss, D. R. MacGorman, E. C. Bruning, V. C. Chmielewski, Two methods for correcting range-dependent limitations of Lightning Mapping Arrays. *J. Atmos. Oceanic Tech.* **35**, 1273-1282 (2018).

49. D. R. MacGorman *et al.*, The electrical structure of two supercell storms during STEPS. *Mon. Wea. Rev.* **133**, 2583-2607 (2005).

50. R. E. Orville, G. R. Huffines, Cloud-to-ground lightning in the United States: NLDN results in the first decade, 1989-98. *Mon. Wea. Rev.* **129**, 1179-1193 (2001).

51. L. D. Carey, S. A. Rutledge, W. A. Peterson, The relationship between severe storm reports and cloud-to-ground lightning polarity in the contiguous United States from 1989-1998. *Mon. Wea. Rev.* **131**, 1211-1228 (2003).

52. I. C. Faloona *et al.*, A laser-induced fluorescence instrument for detecting tropospheric OH and HO_2: characteristics and calibration. *J. Atmos. Chem.* **47**, 139-167 (2004).

53. T. B. Ryerson, E. J. Williams, F. C. Fehsenfeld, An effective photolysis system for fast-response NO_2 measurements. *J. Geophys. Res.* **105(D21)**, 26447-26461 (2000).

54. P. A. Feiner *et al.*, Testing Atmospheric Oxidation in an Alabama Forest, *J. Atmos. Sci.* **73**, 4699-4710 (2016).

55. A. Zahn *et al.*, Electrical discharge source for tropospheric “ozone-rich transients”. *J. Geophys. Res.* **107**, 4638, doi:10.1029/2002JD002345, 2002.

56. G. M. Wolfe, M. R. Marvin, S. J. Roberts, K. R. Travis, J. Liao, The framework for 0-D atmospheric modeling (F0AM) v3.1. *Geosci. Model Dev.* **9**, 3309-3319 (2016).

57. Wolfe, G. M.: F0AM Box Model, available at: https://sites.google.com/site/wolfegm/models (2017).
58. S. M. Saunders, M. E. Jenkin, R. G. Derwent, M. J. Pilling, Protocol for the development of the Master Chemical Mechanism, MCM, v3 (Part A): tropospheric degradation of non-aromatic volatile organic compounds. *Atmos. Chem. Phys.* **3**, 161-180 (2003).
59. M. E. Jenkin, S. M. Saunders, V. Wagner, M. J. Pilling, Protocol for the development of the Master Chemical Mechanism, MCM, v3 (Part B): tropospheric degradation of aromatic volatile organic compounds. *Atmos. Chem. Phys.* **3**, 181-193 (2003).
60. A. Aknan, G. Chen, NASA LaRC Airborne Science Data for Atmospheric Composition – DC3. https://doi.org/10.5067/Aircraft/DC3/DC8/Aerosol-TraceGas (2017).

Acknowledgments: DC3 was sponsored by the U.S. National Science Foundation (NSF), the National Aeronautics and Space Administration (NASA), the National Oceanic and Atmospheric Administration (NOAA), and the Deutsches Zentrum für Luft- und Raumfahrt (DLR). We thank the DC3 scientists, especially I. Pollack, T. Ryerson, and P. Lawson, for the use of their measurements, the DC-8 pilots and operations personnel, the DC3 weather forecasters, and NASA DC3 management for making the DC3 airborne field study possible. **Funding:** NSF award AGS-1834711 supported this work; NASA grant NNX12AB84G supported the collection of the OH and HO_2 data during DC3. **Author contributions:** W.H.B. and P.J.M. performed the formal analysis; W.H.B., D.O.M. X.R., J.M, J.P., E.B., S.W., and D.M. provided DC3 data; W.H.B. and P.J.M. wrote the initial draft; W.H.B., P.J.M., D.O.M., J.M.J., X.R., J.M, J.P., E.B., S.W., and D.M. reviewed and edited the manuscript; W.H.B. supervised the research, analysis, and writing. **Competing interests:** Authors declare no competing interests. **Data and materials**

availability: DC3 data, including the ATHOS 5-Hz OH and HO_2 data, are available at Aknan and Chen, (*60*).

Supplementary Material:

Materials and Methods

Figures S1-S5

Tables S1-S2

Supplementary References 44 - 60

Fig. 1. HO_x abundances (colors, logarithmic scale) along the DC-8 flight track overlaid on LMA flash extent and satellite anvil images during the flight on 22 June, 2012 for three one-hour periods: A. 23:30-00:30; B. 00:30-01:30; C. 01:30-02:30. All times are in UTC. The flash extent locations are shown for the entire hour as the storms moved from west to east. The storm cores are regions of the most intense flash extent (see Supplementary Material for definition).

Fig. 2. Time series of HO_x (blue), NO_x (golden), O_3 (light blue), IWC (light gray), and LMA flash extent (orange) for the time period shown in Fig. 1. **A**. Flash extent are given every minute, whereas 1-Hz NO_x and O_3 data and 5-Hz HO_x data are shown. **B**. The inset expands the region between 00:06:45 and 00:10:00 UTC. OH (green line) has been added to show that OH was often half of HO_x. Black bars below 0 indicate time when HO_x was not being measured. NO_x and O_3 were deemed to be unreliable between 00:16:00 and 00:16:13 and were not reported.

Fig. 3. A lightning flash and LHO_x. **A**. Full frame photograph: lightning captured by the NASA DC-8 forward camera in a deep convection anvil at 00:16:11 UTC on 23 June 2012. **B**. Insert: time series plot of HO_x at 5 Hz (black line) and flash in video (gray vertical line). NO_x and O_3 data were not available during the flash.

Fig. 4. Photochemical box model calculations of the changes in OH, HO_2, NO, and NO_2 for two cases: (a) 00:09:37, no visible flash, with measured values; (b) 00:16:12, visible flash, with assumed values for NO, NO_2, and O_3 consistent with laboratory observations (*26*). (Fig. 3).

Day	Time (UTC)	Peak HO_x (pptv)	Peak OH (pptv)	OH Exposure (10^9 molecules s cm^{-3})	Lightning Visible?
18-May	23:18:34	1661.26	603.38	11.8	No
20-May	00:50:52	439.73	197.38	4.7	No
26-May	01:24:18	229.42	126.04	3.3	No
29-May	23:30:51	586.36	311.19	5.8	No
2-Jun	22:45:18	709.34	309.44	9.9	No
23-Jun	00:09:37	700.53	297.12	9.7	No
23-Jun	00:16:01	890.84	198.15	7.0	Yes
23-Jun	00:16:12	1992.62	334.34	1.2	Yes
23-Jun	00:56:27	1984.12	472.15	6.2	No

Table 1. Major HO_x peaks and resulting modeled OH exposure from six flights. These observed peaks may be lower than initially generated peaks because the sampling is probably not always coincident with the electrical discharge.

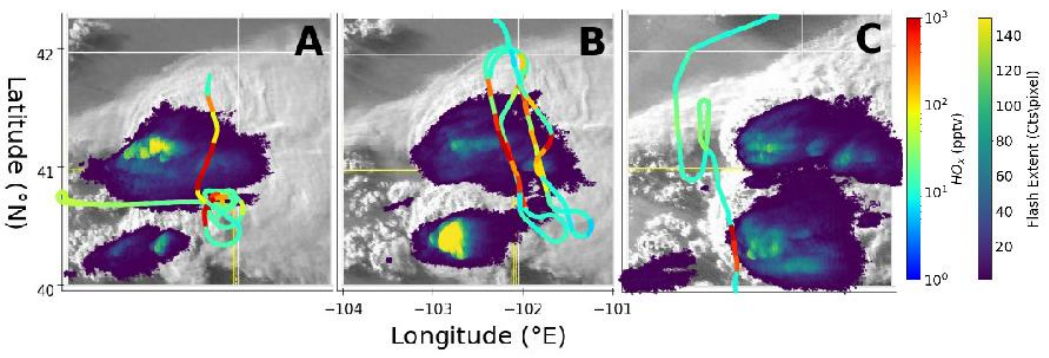
A
B
C
42
41
40
Latitude (°N)
−104
−103
−102
−101
Longitude (°E)
10^3
10^2
10^1
10^0
HO_x (pptv)
140
120
100
80
60
40
20
Flash Extent (Cts/pixel)

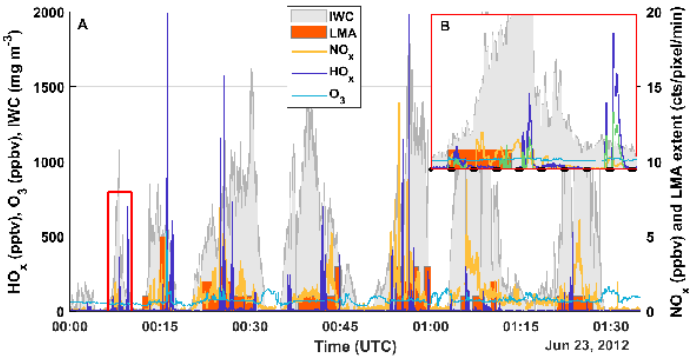
A
B
IWC
LMA
NOx
HOx
O3
2000
1500
1000
500
0
20
15
10
5
0
00:00
00:15
00:30
00:45
01:00
01:15
01:30
Time (UTC)
Jun 23, 2012
HOx (pptv), O3 (ppbv), IWC (mg m-3)
NOx (ppbv) and LMA extent (cts/pixel/min)

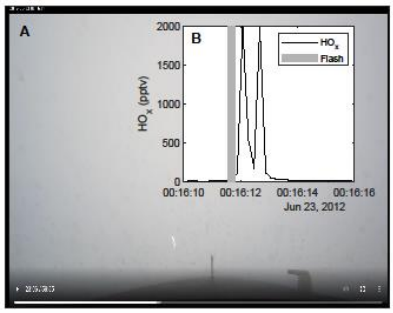
A
B
2000
1500
1000
500
0
HO_x (pptv)
HO_x
Flash
00:16:10
00:16:12
00:16:14
00:16:16
Jun 23, 2012

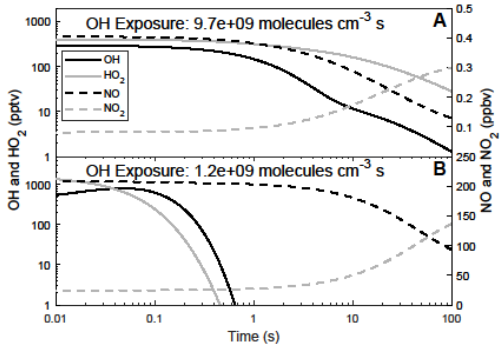
OH Exposure: 9.7e+09 molecules cm-3 s
A
OH
HO2
NO
NO2
OH Exposure: 1.2e+09 molecules cm-3 s
B
OH and HO2 (pptv)
NO and NO2 (ppbv)
Time (s)

Supplementary Materials for

Extreme Oxidant Amounts Produced by Lightning in Storm Clouds

W. H. Brune, P. J. McFarland, E. Bruning, S. Waugh, D. MacGorman, D. O. Miller, J. M. Jenkins, X. Ren, J. Mao, J. Peischel

Correspondence to: whb2@psu.edu

This section includes:

Materials and Methods
References 44 to 60
Figs. S1 to S4
Table S1 to S2

Materials and Methods

The DC3 campaign collected data on 32 different flights over the course of May and June 2012 (*29*). Of those cases, six were chosen for this study based on measurement of enhanced HO_x (HO_x = OH + HO_2) and the DC-8 aircraft flying through an anvil of deep convection that was being observed by a Lightning Mapping Array (LMA). Three of the chosen cases were flights over northeastern Colorado: 18 May, 2 June, and 22 June, while the remaining three cases were over central Oklahoma or northern Texas: 19 May, 25 May, and 29 May. We focus mainly on the 22 June case in this paper because several passes were made through the anvil on that flight, more than on any other flight. Specifics on the aircraft payloads and ground network setups of the DC3 regions can be found in Barth et al. (*29*). The following sections detail how each type of data used in this study was obtained and analyzed.

The Lightning Mapping Array

A lightning mapping array (LMA) is a system of sensors that detects very high frequency (VHF) radiation emitted by lightning segments as it propagates along its path (*32,44,45*). Typically, LMAs consist of at least eight independent sensors arranged in a 50-100 km. diameter circle around a central sensor. The system is tuned to detect VHF radiation in an unused local television band (generally 60-66 MHz) to avoid signal interference from other sources (*45*). Using GPS and the VHF radiation time-of-arrival across multiple stations, VHF signals are recorded, and their sources are mapped in time and space (*32,34*). Additional details on the nuances of the LMA can be found in Thomas et al. (*34*).

The two LMAs from which lightning data was retrieved for this study are the Colorado LMA (COLMA) and the Oklahoma LMA (OKLMA). The COLMA network is larger than most LMAs, with a diameter of roughly 100 km, which gives a serviceability radius of about 350 km around the system (*46*). This network has been found to be quite accurate, with little to no flash distortion out to 125 km from the LMA center (*32*). Conversely, the OKLMA works to only approximately 250 km from the system due in part to its smaller diameter. As a result, range errors were much larger at distances greater than 200 km for OKLMA than for COLMA.

Raw LMA data for each of the cases examined in this study was retrieved from the public DC3 data site (https://data.eol.ucar.edu/master_lists/generated/dc3/). A Density-Based Spatial Clustering of Applications with Noise (DBSCAN) program, developed in the python programming language, was used to sort and grid the raw LMA data into individual lightning flashes (*44*). The application is publicly available and can be downloaded at https://github.com/deeplycloudy/lmatools. This software identifies lightning by first locating a random VHF source detected by the LMA (*45*). The DBSCAN algorithm then searches for at least nine additional VHF sources within 3 km in space and 150 ms in time of the initial source, forming a VHF cluster (*46*). Once a cluster with sufficient sources has been identified, it is then checked against the number of LMA stations that recorded a VHF signal within the cluster. If at least six of the individual LMA stations within the network recorded a VHF source within the identified cluster, the cluster is categorized as a flash, which is assigned to be a single point in space and time and saved. The cluster is also gridded in the four dimensions of time, latitude, longitude, and altitude (*45,46*). Each grid pixel within this grid is roughly square with a spatial extent of approximately 1 km in latitude, longitude, and altitude, and a timestep of 1 minute. This filtering process is repeated until all the VHF sources have been classified as either lightning or noise.

The program outputs information on seven flash characteristics: flash extent (count $pixel^{-1}$ min^{-1}), flash initiation (count $pixel^{-1}$ min^{-1}), source density (count $pixel^{-1}$ min^{-1}), flash area/footprint (km^2 $flash^{-1}$), flash size standard deviation (count $pixel^{-1}$ min^{-1}), specific energy (J kg^{-1} $flash^{-1}$), and total energy (J $flash^{-1}$). The flash extent counts the number of flashes that pass through each grid pixel in a minute. A single flash passes through multiple grid cells, making flash extent a reliable variable for determining the total area of electrical activity. Unlike flash extent, flash initiation only counts the grid cell from which the flash originated. Flash initiation can therefore be summed up to count the number of individual flashes detected by the LMA each minute. Source density depicts where the VHF sources from valid flashes are located. It does not resolve these sources into flashes as is done for the other flash characteristics. Flash footprint is the average area of a flash and is calculated as the sum of the areas of each flash that passes through a grid cell divided by the flash extent value for that grid cell. Flash size standard deviation is simply the standard deviation of this area calculation. Total energy is the estimated electrostatic energy neutralized by a flash, and specific energy is this same value divided by the air density at the altitude at which the flash originated.

For this study, flash extent (FE) was chosen as the variable of interest. This characteristic was chosen over others because a recent study found that FE may be more representative of lightning than other flash characteristics, which tend to be restricted to regions with radar reflectivity dBZ values >20, known as the 20-dBZ echo volume (*47*). In addition, FE can only take integer values, which makes it is easier to interpret, as it can be thought of as an on/off switch for lightning

The LMA volume was determined as follows. Wherever FE values are greater than zero, a flash passed through that grid cell, and the assumption is made that the entire 1 km^3 grid cell was electrically favorable for lightning. Conversely, where FE vales are zero, no flash passed through that grid cell and the entire cell is assumed to be unfavorable for electrical discharges. The LMA volume is the total volume of all the grid cells with FE greater than 0 for any given second.

Analysis of DC3 LMA data

After creating the four-dimensional FE files from the DBSCAN software, the LMA data was compared to the data collected aboard the DC-8 aircraft. By matching the timestamps of the two different datasets, FE and HO_x were compared on a minute-by-minute basis. The maximum FE value within each minute of the 5 Hz HO_x data was used to make this comparison. The aircraft's location was used to locate which FE grid cells it was flying through. Because the aircraft traveled at an estimated speed of 12 km min^{-1}, the plane traversed several grid cells each minute.

To account for any small errors in the LMA gridding process, any grid cells within 0.02° latitude and longitude or 1 km altitude were also included in the region the plane flew through.
These values were chosen because they could be standardized for all six cases analyzed in this study despite the differences in error values between the two LMAs. Some cases, such as the 22 June and 29 May, stayed well within the range of the LMA for the entire duration of the flight, and this surrounding area could be decreased to within 0.005° latitude and longitude while still detecting the same number of flashes. Other cases, such as 18 May spent significant time on the limits of or outside of the LMA range, and thus required consideration of a larger surrounding area. However, this distance became problematic when the DC-8 reentered the LMA region and this large area began to pick up on flashes at times when there was no significant HO_x, NO_x, or O_3 spike. Thus, 0.02° was used to maximize the area of consideration surrounding the DC-8 while simultaneously minimizing the number of these erroneous flashes.

Typically, 20 grid cells were identified as being active for each timestep. The 18 May case in Colorado was the only one to use different threshold values of 0.06° latitude and longitude and 1 km altitude due to the plane being more than 350 km (and nearly out of range) from the COLMA when the HO_x spikes were recorded. Once all the surrounding grid cells were identified, the maximum FE value among them was selected to avoid unnecessary dilution via averaging. For the purposes of this study, FE is used to indicate whether lightning was present near the aircraft location or not, and only one of the six cases analyzed (22 June) had FE values that exceeded one. After repeating this process for each minute of a flight, the HO_x data and lightning data were plotted against time to determine if a spike in the HO_x mixing ratio occurred at the same time a flash was identified near the location of the aircraft (see **Fig. 3**).

LMA Uncertainty and Limitations

The LMA has some limitations that are relevant to this study. First, LMA detection efficiency decreases while flash location errors increase with increasing distance from the network (*32*,*44*), and the range errors increase more than azimuth errors. Range errors increase at a rate proportional to $(r/D)^2$, where r is the radial distance from the center of the LMA, and D is the diameter of the LMA. Therefore, the area over which an LMA is serviceable greatly depends on its diameter. Altitude errors also increase with range, and tend to have a high bias of a few hundred meters at 100s of km range. Together, these effects explain at least some of the the radial stretching of the three clusters of VHF sources along the DC-8 flight track and the position of the VHF sources generally above the aircraft track altitude. This range limitation becomes an issue as the aircraft follows storms as they move from in to out of the LMA range. LMAs generally have a serviceability radius of a few hundred km (*34*), so a storm that stays within that range for several hours is no easy feat.

Another limitation is the LMA's power lower threshold. Generally, LMAs have lower power thresholds set around -70 to -80 dBm, so that noise from power lines or electronic equipment are not falsely detected as lightning (*34*). However, this threshold can also prevent detection of low-energy and subvisible flashes. Lightning discharge power decreases according to the inverse square law, so weak flashes associated with supercell

thunderstorms or low power corona-like discharges that are far from the LMA are highly unlikely to be detected (*45*,*48*). As a result, the LMA likely missed some of the low-energy and subvisible flashes.

Finally, positive flash channels tend to emit a more continuous and weak VHF signal than negative flashes (*49*). This tendency is a potential issue for the three Oklahoma cases analyzed in this study because any positive channels would be much less likely to be detected, especially at the longer ranges observed in this study (*50*,*51*). As a result, the LMA may completely miss the presence of positive flashes despite their being located well within the LMA's serviceable range (*49*).

Measurements of OH, HO_2, NO, NO_2, and O_3

HO_x (HO_x = OH + HO_2) mixing ratios measured in parts per trillion by volume (pptv) were collected via laser-induced fluorescence (LIF) by the Penn State Airborne Tropospheric Hydrogen Oxides Sensor (ATHOS) (*52*). Air is pulled by a vacuum pump through a 1.5 mm diameter inlet, down a detection tube, and through the OH detection axis and then the HO_2 detection axis. In the detection axes, a laser beam (3-kHz repetition rate, 20-ns pulses length) is passed 32 times over the detection region. The laser radiation gets absorbed by OH, which then fluoresces. This fluorescence is detected with a gain-gated microchannel plate set at right angles to the laser path. In the first 100 ns during and after the laser pulse, the detector gain is off to allow scattering of laser radiation from air, the walls, and cloud particles to subside. From 150 to 700 ns after the laser pulse, the gain is turned on so that the detector can measure the weak OH fluorescence. Between the two detection axes, nitric oxide (NO) is added to convert HO_2 to OH, which is then detected in the second detection axis. The laser radiation wavelength is set to be in resonance with OH (or online) for 15 seconds, and then off resonance with OH (or offline) for 5 seconds, resulting in a 20 second total time resolution. The OH fluorescence signal is calculated as the difference between the online and offline values.

The OH and HO_2 detection axes are calibrated in the laboratory and the calibration is maintained in flight by monitors of laser power, on-line wavelength position, pressure, temperature, and scattering signals. The absolute uncertainty was estimated to be $\pm$16% for both OH and HO_2 at a 68% confidence level. The 1σ precision for a 1-min integration time during this campaign was about 0.01 pptv for OH and 0.1 pptv for HO_2 (*30*).

OH and HO_2 mixing ratios are typically reported every 20 seconds so as to improve the signal-to-noise ratio for OH, even though all the measurements and housekeeping data for ATHOS are recorded at 5 Hz. During the preparation of the DC3 OH and HO_2 data for the analysis reported in Brune et al. (*30*), a few OH and HO_2 spikes were noted in the 20-second data, but they were infrequent and assumed to be instrument artifacts. As such, they were set aside for later analysis and not included in the published results. Only when the raw 5-Hz data were later examined did it become clear that these large spikes were due to atmospheric OH and HO_2 and not instrument artifacts.

To convert the 5-Hz detector counts into mixing ratios, the calibration factors determined for the 20-second data were interpolated to the 5-Hz time stamp and applied to both on-line and off-line signals. The off-line signals, which were typically 0.2 cts s^{-1} and as much as 10 cts s^{-1} in dense clouds, were much smaller than the online signals of hundreds to thousands of counts and not subtracted. The time between the air entering the ATHOS inlet and the OH detection is 20 ms, so the possible time lag of the OH and HO_2 measurements is less 0.2 seconds, the electronic sampling integration time.

NO_x (NO_x = NO +NO_2), and O_3 mixing ratios reported in parts per billion by volume (ppbv) were measured using chemiluminescence by the National Oceanic and Atmospheric Administration (NOAA) Chemical Sciences Laboratory Chemiluminescence instrument (CSL CL). Details on this method of measurement can be found in Ryerson et al. (*53*) and Pollack et al. (*17*). The CSL CL collected data at a frequency of 1 Hz and a time lag relative to the HO_x measurements of 1.6$\pm$0.3 s, as determined by lining up the observed spikes in HO_x and NO_x.

The CSL CL sometimes experienced identifiable electrical interferences while in the electrified anvil, thus causing the NO_x measurements to be deemed unreliable. Unfortunately, this interference tended to occur when the DC-8 entered more electrified regions in the anvil, particularly near lightning flashes. This lack of NO_x and O_3 data complicated the chemical modeling of the greatly enhanced HO_x observations that were caused by those flashes. Therefore, in order to calculate the OH exposure for the enhanced HO_x that followed the lightning flashes directly in front of the DC-8 on 23 June at 00:16:11, we initialized the photochemical box model with NO, NO_2, and O_3 values typically observed in laboratory for weak lightning flashes (*26*).

The CSL CL inlet was located on the port side and the ATHOS inlet was located underneath the aircraft, 2.5 m behind the CSL CL inlet. When the aircraft is viewed from its nose, the two inlets were separated by 3.5 m. The rapid, large change in the HO_x data, shown in Fig. 3 (insert), occurs at 5-Hz frequency, which is equivalent to ~40 m, so that substantial gradients in HO_x and possibly NO_x were occurring over a few meters. It is therefore

possible that the two inlets might not be sampling air affected by the same segments of the lighting flashes or subvisible electrified regions.

Tests demonstrating that these enhanced HO_x signals are not instrument artifacts

Could these extreme OH and HO_2 enhancements be artifacts of the laser induced fluorescence instrument? The evidence says "No". First, the large HO_x signals were seen only when the laser wavelength was in resonance with the OH absorption and were otherwise equal to the typical background signal (e.g., **Fig. 2**, inset, far right). Second, if the HO_x signals were interference signals, as have been seen only in the presence of O_3 and alkenes (*54*), then we would expect that they would also occur when the DC-8 flew through the smoke plume filled with NO_x and VOCs that was being ingested into the convection on 23 June. However, they did not. The measured OH was below 0.1 pptv and measured HO_2 was below 17 pptv, agreeing with modeled OH and HO_2 to within uncertainties. Third, ATHOS records the OH fluorescence signals in 50-ns bins and the decay of the signals in bins increasingly later than the laser pulse is consistent with the expected OH signal decay due to the OH fluorescence lifetime and quenching by humid air. Finally, our laboratory studies demonstrate that enhanced OH and HO_2 are generated by electrical discharges, even subvisible ones, and that the observed enhanced HO_x amounts are similar for the laboratory and DC3 (*26*).

It has been suggested that flashes or corona can be initiated on airborne instrument inlets, producing artifact signals (*13*,*55*) or even on aircraft (*34*). The possibility of corona or spark generation on the ATHOS inlet or on the DC-8 does not alter the conclusion that electrical discharges produce enhanced HO_x, but it would affect calculations of the amount of HO_x being produced in a storm. Several observations and tests were used to examine the possibility that the observed enhanced HO_x was due to sparks, corona, or subvisible discharges on the ATHOS inlet or the DC-8.

For sparks or corona on the inlet, the first piece of evidence is that a visible spark or corona on the ATHOS inlet would have been observed by the UV photodiode mounted in the ATHOS nacelle wall. This photodiode observes the ATHOS inlet near the center of its wide field-of-view and has a signal-to-noise ratio of 50-100 for scattered solar UV radiation (**Fig. S2**). In a laboratory test, a weak spark anywhere within 20 cm of the inlet gave a signal comparable to the solar UV signals observed in DC3 (**Fig. S2**). However, the nacelle UV sensor did not detect any of the three flashes observed in front of the aircraft on 23 June nor any flashes or corona at times corresponding to enhanced HO_x, indicating that neither flashes nor coronal discharges on the ATHOS inlet could be responsible for the enhanced HO_x at those times.

On 29 May at 23:51:44 UTC, enhanced HO_x, lightning flashes, and a small UV signal (<5% of typical solar signal) were simultaneously observed. The aircraft had entered an electrified region and encountered lightning flashes, including one that punched a 1-cm hole in the right rear stabilizer. However, this UV signal was so small that it must have come from flashes around the aircraft and not on the ATHOS inlet. A close examination of the LMA flashes as a function of time shows the initial flashes occurring several kilometers above and in front of the DC-8 and subsequent flashes progressing toward the DC-8 and engulfing it.

The second piece of evidence comes from a laboratory simulation of a spark striking the ATHOS inlet. Two electrodes - one attached to a Tesla coil and the other to ground – were set 1 cm apart in a plane that was ~0.4 cm from the inlet surface. The Tesla coil spark energy was adjusted to an energy value so low that no spark or enhanced HO_x occurred when the electrodes were 4 cm upwind from the inlet in the plane. The electrodes were then moved parallel to the plane and positioned near the center of the inlet. Sparks occasionally occurred between the electrode attached to the Tesla coil and the grounded ATHOS inlet. These sparks produced sharp enhanced HO_x peaks of a several hundred pptv, but they also caused small distinctive spikes (i.e., sharp rise and one-second decay) in the recorded voltage of the high voltage power supply for the ATHOS microchannel plate detectors. The signal-to-noise for these peaks was greater than 10. No such signals were observed on the high voltage during DC3 for any of times when HO_x was enhanced during DC3.

We also consider corona on the DC-8 aircraft body as causing the enhanced HO_x. The ATHOS inlet is 53 cm below the underside of the DC-8, 10 m from the tip of the DC-8 nose. With the nose wheel is up, the only other significant structure in front of the ATHOS inlet is a blade antenna, ~3-5 cm wide and 45 cm long, located 380 cm in front of the ATHOS inlet. During the flight in the anvil on 23 June, the DC-8 was pitched up 2^o, which is typical. As a result, there was no aircraft structure within 20 cm of the clear air stream being sampled by the ATHOS inlet. Furthermore, none of the structures seen in the forward camera (**Fig. 3**) show any evidence of corona, even when close to lightning.

To examine the possibility that the subvisible discharges were caused by the ATHOS inlet distorting and intensifying the electric field, we used the same laboratory procedure as for the inlet sparking test above. In this case, the electrodes were set 4 cm upstream from the inlet and in a plane that was 1 cm from the inlet surface. Tesla

coil energy was set so that no sparks occurred but subvisible electrical discharges produced several hundred pptv of OH. The electrodes were then moved in the plane to a position over the inlet and 0.4 mm upwind of the inlet sampling hole. The signal at 4 cm was about half the signal at 0.4 cm away from the inlet, but this decrease is consistent with the expected decrease in OH mixing ratios due to diffusion and chemical loss between the two positions.

Then the Tesla coil energy was adjusted lower so that enhanced OH signals were only occasionally observed. In this case, the electric fields were so weak that the observed OH was never more than a few pptv, but the small enhanced OH was greatest when the electrodes were near the inlet and then decreased when they were 4 cm away. This test suggests that it is possible for the ATHOS inlet to distort and enhance the electric field enough to produce small amounts of OH, but only for limited and insignificant circumstances.

Thus, we can rule out the enhanced HO_x coming from flashes, corona, or subvisible discharges on the ATHOS inlet or on the DC-8 aircraft.

It is possible that the DC-8 itself induced the lightning flashes or the subvisible discharges, even out in front of it by tens of meters, by distorting and intensifying the electric field. The behavior of the lightning flashes in **Fig. S1** suggest that the DC-8 might be having some influence on lightning flash initiation in this case, but it is far from conclusive. This hypothesis needs more research.

Photochemical Box Model

The Framework for 0-D Atmospheric Modeling (F0AM) is a photochemical box model developed in the MATLAB coding language that simulates OH and HO_2 at a single point in space (*56*). F0AM is publicly available at Wolfe et al. (*57*). Because all the chemical reactions modeled in this study occur in the gas phase, the Master Chemical Mechanism v.3.3.1 was used (*58,59*). The model was initialized with molecule mixing ratios for OH, HO_2, NO, NO_2, O_3, CO, CH_4, formaldehyde, acetaldehyde, hydrogen peroxide, methyl hydroperoxide, and other trace gases that account for more than 95% of the total OH reactivity calculated with the complete set of DC3 measurements (*30*) for the times of chosen HO_x enhancements. These data are publicly available (*60*).

In **Fig. 4**, the calculated OH and HO_2 evolution with time is presented for two enhanced HO_x peaks observed on 23 June. For the first case at 00:09:37, no visible flash was observed and the model was initialized with 0.5 ppbv of NO_x, 70 ppbv of O_3, 1804 ppbv of methane (CH_4), 76 ppbv of carbon monoxide (CO), 0.1 ppbv of formaldehyde (HCHO), other chemical species to account for 95% of the OH reactivity calculated with the complete set of DC3 measurements, and 700 pptv of HO_x. For the second case at 00:16:11, the DC-8 sampled the air affected by the visible flash in **Fig. 3** and the model was initialized with 230 ppbv of NO_x and 400 ppbv of O_3, which were estimated from laboratory measurements, and a measured 1840 ppbv of CH_4, 200 ppbv of CO, 2.6 ppbv of HCHO, other chemical species to account for 95% of the OH reactivity calculated with the complete set of DC3 measurements, and 2000 pptv of HO_x. The model was also constrained by measured environmental conditions including photolysis frequencies (*30*).

F0AM was then run for 120 seconds with no further inputs. OH exposure, or the integral of the OH exposure with respect to time, was then calculated from the model output by Eq. 1.

Two pieces of evidence demonstrate that the model is correctly calculating OH exposure. First, during DC3, the modeled and observed OH agree to well within the combined uncertainties of the model and measurement, even in the non-electrified parts of the anvils. Thus, the model can simulate the normal amounts of atmospheric OH. Second, we modeled the laboratory experiments of the OH decays that occurred after subvisible discharges, which are more relevant to the DC3 observations than laboratory experiments with sparks that produce ppmv levels of NO. This model, which was used to calculate the OH exposures for DC3, was constrained by the laboratory flow tube temperature, pressure, water vapor, NO, NO_2, O_3, CO, CO_2, and OH reactivity (*26*). It was able to simulate the observed OH and HO_2 decays in these laboratory experiments. Thus, we have confidence in the DC3 model results for OH exposure.

Estimation methods for storm and global OH from LHO_x

Estimation method #1: counting flashes

The OH exposure for one second equals the OH concentration for that one second. For each visible flash or subvisible electrical discharge, a certain amount of OH exposure is generated. To get the total amount generated per second for a storm, we use the Equation S1.

$$[OH]_{storm} = F_{storm}\, V_{LMA}\, f_{LHOx}^{sec}\, r_{vis}^{tot}\, OH_{exp} \quad \text{Eq. S1}$$

F_{storm} is the flash rate per storm, found by adding up all the LMA flash initiation values and dividing by the storm duration (flash s^{-1} $storm^{-1}$); V_{LMA} is the mean LMA volume (cm^3), found by counting the number of 1 km^3 grid boxes with flash extent values greater than 0 for each minute; f_{LHOx}^{sec} is the number of measurements of enhanced HO_x, that is sampled within 1 second of when it was generated divided by the number of measurements in the regions where the LMA detected flashes; r_{vis}^{tot} is the ratio of the total enhanced HO_x produced within the past second, both in and out of the regions where the LMA detected flashes but still within the anvil, to the enhanced HO_x observed to be produced by a lightning flash within the past second along the same flight path; and OH_{exp} per flash is the OH exposure (molecules cm^{-3} s $flash^{-1}$), found from photochemical box model calculations using initial conditions from the DC-8 data for several different LHO_x peaks (**Table S2**).

For HO_x generated by the subvisible discharges, the initial OH/HO_x ratio appears to be 0.5, while for the observed visible flashes it is below 0.35. A series of box model runs for the conditions of different observed HO_x peaks from subvisible discharges with initial OH/HO_x ratios set to 0.5 show that this ratio falls to 0.35 in ~1 second. f_{LHOx}^{sec} is the fraction of enhanced HO_x values that has OH/HO_x greater than 0.35 (0.25-0.45). For r_{vis}^{tot}, the subvisible enhanced HO_x is found by filtering for the fraction of enhanced HO_x values that has OH/HO_x greater than 0.35 (0.25-0.45) and NO_x levels below the mean NO_x background in the anvil outside of enhanced HO_x regions, or 0.6 ± 0.3 ppbv. The enhanced HO_x generated by visible flashes is found by filtering for $OH/HO_x < 0.35$ (0.25-0.45) and $HO_x > 1000$ (800-1200) pptv.

For the 22-23 June convective cell, F_{storm}= 0.8 (0.4-1.2) flashes s^{-1} $storm^{-1}$, V_{LMA} = $1x10^{17}$ ($0.71\text{-}1.3x10^{17}$) cm^3, f_{LHOx}^{sec} = 0.02 (0.01 – 0.03), r_{vis}^{tot} = 16 (5 – 25), OH_{exp} is the weighted average of OH_{exp} = $1.2x10^9$ molecules cm^{-3} s $flash^{-1}$ in the visible flash, and OH_{exp} = $9.7x10^9$ ($5.0\text{-}14.2x10^9$) molecules cm^{-3} s subvisible $discharge^{-1}$, using r_{vis}^{tot} to establish the weighting. This value for the OH exposure per flash was chosen because it was calculated for one of the enhanced HO_x peaks that meets the criteria for having been generated in the past 1 second, which occurred on 23 June at 00:09:37. The OH generated by LHO_x for each second that this storm was active was $2.7x10^{26}$ molecules.

Estimation method #2: LHO_x along the DC-8 flight track

We assume the measured variables along the DC-8 flight track through the anvil are representative of the electrically active anvil volume. To get the total amount generated per second for a storm, we use the Eq. S2.

$$[OH]_{storm} = V_{LMA}\, f_{LHOx}^{sec}\, r_{LMA}^{anvil}\, OH_{exp} \quad \text{Eq. S2}$$

V_{LMA} is the mean LMA volume (cm^3); f_{LHOx}^{sec} is the number of measurements of enhanced HO_x that is sampled within 1 second of when it was generated divided by the number of measurements in the regions where the LMA detected electrical discharges; r_{LMA}^{anvil} is the ratio of the amount of enhanced HO_x along the DC-8 flight track in the anvil to the amount along the DC-8 flight track in the LMA region; and OH_{exp} per discharge is the same as in Method 1. Note that V_{LMA}, f_{LHOx}^{sec}, and OH_{exp} are used in both Eq. S1 and Eq. S2, with only one term being different between the two equations.

For the 22 June convective cell, the LMA volume was $1x10^{17}$ ($7.1 – 1.3x10^{17}$) cm^3, f_{LHOx}^{sec} was 0.02 (0.01-0.03), r_{LMA}^{anvil} was 1.4 (1.1-1.7), and the OH exposure per flash was $9.7x10^9$ ($6.3\text{-}14.2x10^9$) molecules cm^{-3} s $flash^{-1}$. The OH generated by LHO_x for each second in the anvil of this convective cell was active was $3.1x10^{25}$ molecules.

<u>Extrapolation to global OH from LHO_x</u>

Assuming that this convective cell on 22 July is typical, the global [OH] for each second from LHO_x requires only multiplying by the number of electrically active convective cells for each second, on average, which is taken to be 1800 (*16*). This calculation is repeated for the 29 May storm as well. For the other three storms, the DC-8 did not sample enough of the electrified anvil within range of an LMA to determine storm or global OH from LHO_x.

<u>Uncertainty estimation</u>

The ranges in the terms in Eq. S1 and Eq. S2 are large, suggesting that the uncertainty in the calculated OH generated by LHO_x will be large. To determine the uncertainty, we randomized the values of the terms in Eq. S1 and

Eq. S2 over the ranges of values presented the section "Estimations of storm and global OH from LHO_x". For some variables, we assumed equal probability over a range of possible values given in parentheses. For a few variables, a normal distribution was assumed and the range is given in terms of a standard deviation. We then performed a Monte Carlo simulation with 100,000 calculations of the OH generated by LHO_x for each second in an electrically active convective cell and the percentage of the total global OH that is estimated to be generated by LHO_x. The results are shown in the violin plot in **Fig. S5**.

Supplementary References

61. E. C. Bruning, Streamed clustering of lightning mapping data in Python using sklearn, presented at 12th Python in Science Conference (SciPy), Austin, TX, June 2013.
62. B. R. Fuchs *et al.*, Climatological analysis of LMA data with an open-source lightning flash-clustering algorithm. *J. Geophys. Res. Atmos*, **121**, 8625-8648 (2016).
63. B. M. Basarab, S. A. Rutledge, B. R. Fuchs, An improved lightning flash rate parameterization developed from Colorado DC3 thunderstorm data for use in cloud-resolving chemical transport models. *J. Geophys. Res. Atmos.* **120**, 9481-9499 (2015).
64. T. C. Davis, S. A. Rutledge, B. R. Fuchs, Lightning location, NO_x production, and transport by anomalous and normal polarity thunderstorms. *J. Geophys. Res. Atmos.* **124**, 8722-8742 (2019).
65. S. A. Weiss, D. R. MacGorman, E. C. Bruning, V. C. Chmielewski, Two methods for correcting range-dependent limitations of Lightning Mapping Arrays. *J. Atmos. Oceanic Tech.* **35**, 1273-1282 (2018).
66. D. R. MacGorman *et al.*, The electrical structure of two supercell storms during STEPS. *Mon. Wea. Rev.* **133**, 2583-2607 (2005).
67. R. E. Orville, G. R. Huffines, Cloud-to-ground lightning in the United States: NLDN results in the first decade, 1989-98. *Mon. Wea. Rev.* **129**, 1179-1193 (2001).
68. L. D. Carey, S. A. Rutledge, W. A. Peterson, The relationship between severe storm reports and cloud-to-ground lightning polarity in the contiguous United States from 1989-1998. *Mon. Wea. Rev.* **131**, 1211-1228 (2003).
69. I. C. Faloona *et al.*, A laser-induced fluorescence instrument for detecting tropospheric OH and HO_2: characteristics and calibration. *J. Atmos. Chem.* **47**, 139-167 (2004).
70. T. B. Ryerson, E. J. Williams, F. C. Fehsenfeld, An effective photolysis system for fast-response NO_2 measurements. *J. Geophys. Res.* **105(D21)**, 26447-26461 (2000).
71. P. A. Feiner *et al.*, Testing Atmospheric Oxidation in an Alabama Forest, *J. Atmos. Sci.* **73**, 4699-4710 (2016).
72. A. Zahn *et al.*, Electrical discharge source for tropospheric "ozone-rich transients". *J. Geophys. Res.* **107**, 4638, doi:10.1029/2002JD002345, 2002.
73. G. M. Wolfe, M. R. Marvin, S. J. Roberts, K. R. Travis, J. Liao, The framework for 0-D atmospheric modeling (F0AM) v3.1. *Geosci. Model Dev.* **9**, 3309-3319 (2016).
74. Wolfe, G. M.: F0AM Box Model, available at: https://sites.google.com/site/wolfegm/models (2017).
75. S. M. Saunders, M. E. Jenkin, R. G. Derwent, M. J. Pilling, Protocol for the development of the Master Chemical Mechanism, MCM, v3 (Part A): tropospheric degradation of non-aromatic volatile organic compounds. *Atmos. Chem. Phys.* **3**, 161-180 (2003).
76. M. E. Jenkin, S. M. Saunders, V. Wagner, M. J. Pilling, Protocol for the development of the Master Chemical Mechanism, MCM, v3 (Part B): tropospheric degradation of aromatic volatile organic compounds. *Atmos. Chem. Phys.* **3**, 181-193 (2003).
77. A. Aknan, G. Chen, NASA LaRC Airborne Science Data for Atmospheric Composition – DC3. https://doi.org/10.5067/Aircraft/DC3/DC8/Aerosol-TraceGas (2017).

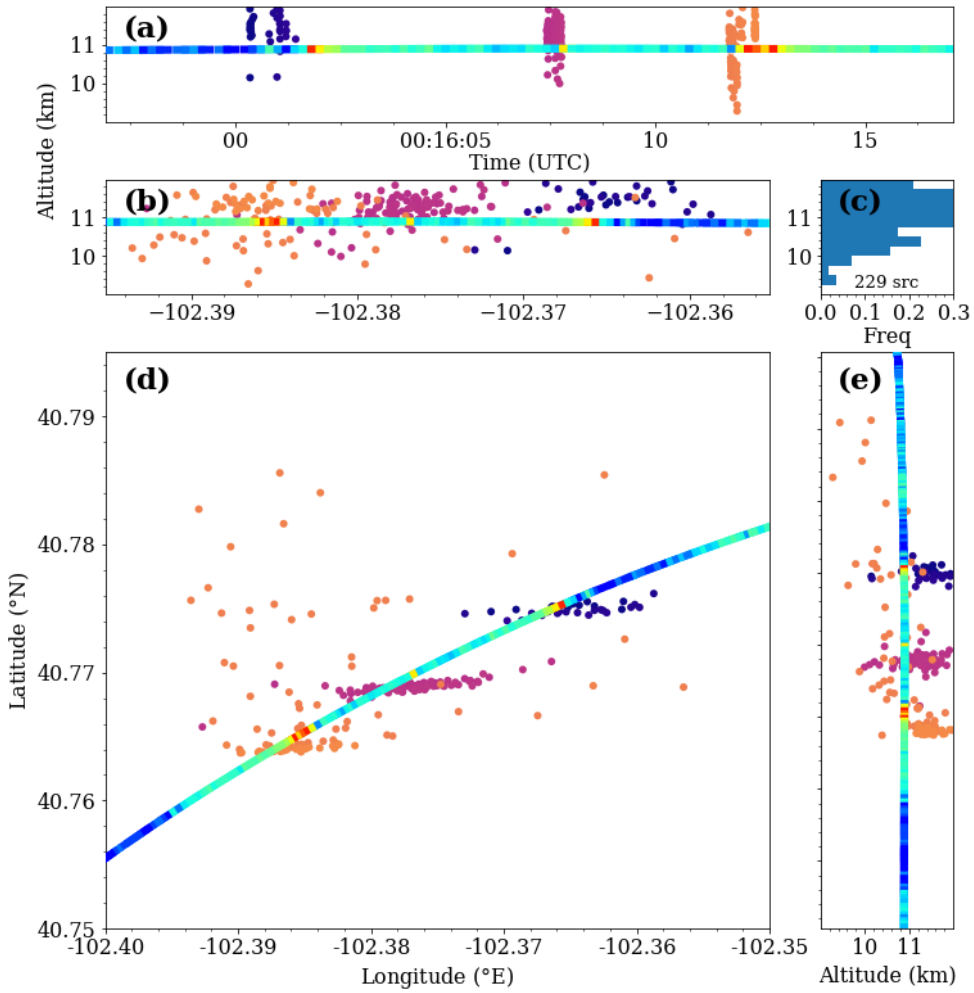

Fig. S1. LMA flash observations near the aircraft track on 23 June from 00:16:00 to 00:16:15 UTC as a function of time and altitude (a), longitude and altitude (b), and longitude and latitude (c). The lightning flashes precede the HO_x spikes in time (a), but they coincide with the HO_x spikes they caused in space (b and c). For instance, the cluster of sources at 16:00:00.2 likely cause the first HO_x peak (red section on aircraft track) because in b and c, the DC-8 gets closer to that cluster of flashes than to the other flashes for the time period. For the enhanced HO_x at 00:16:11.8, note that a flash appears to be only a few tenths of a seconds before for the spike, and seems to be slightly to the left and above the aircraft from (b) and (d). This position is consistent with the DC-8 forward camera photograph in **Fig. 3**.

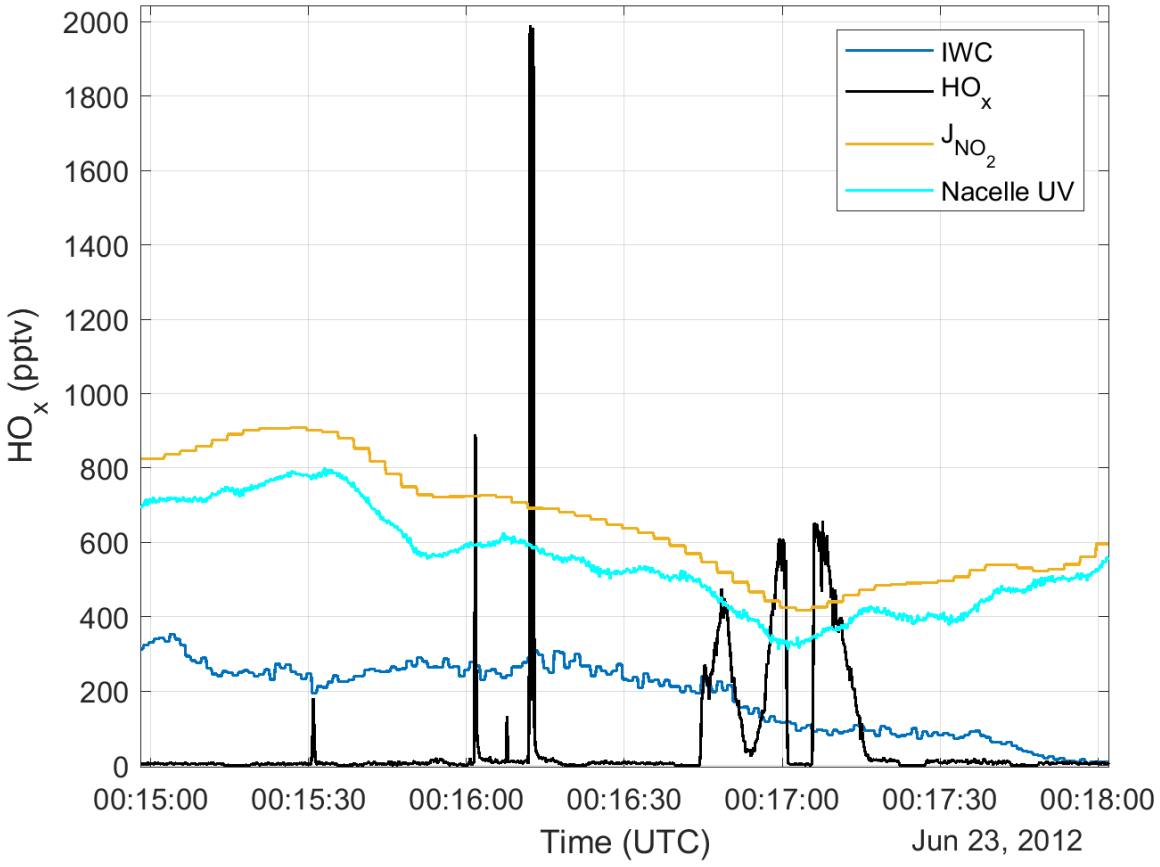

Fig. S2.

Enhanced HO_x (black line), ice water content (blue line), NO_2 photolysis rate (gold line), and nacelle photodiode signal (cyan line) versus time of day for June 22, 2012. HO_x is in pptv; all others are scaled. The nacelle photodiode detects scattered solar UV radiation, but shows no evidence of a visible spark or corona on the ATHOS inlet even during times of enhanced HO_x.

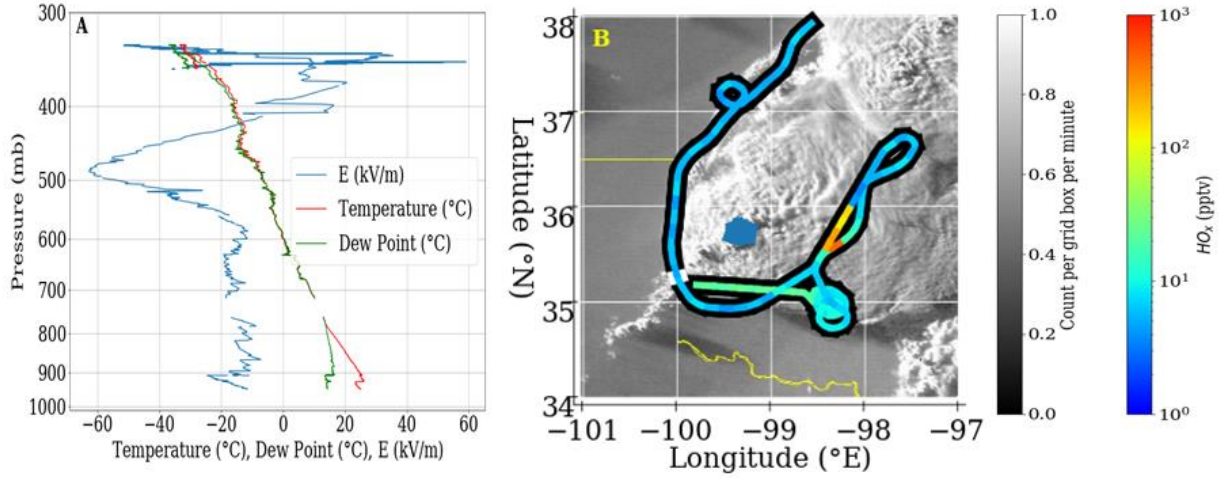

Fig. S3.

Electric field sounding and its corresponding location on May 19. **Fig. S2-A** (left) depicts temperature (red line), dew point (green line) and the local electric field (blue line) recorded during a balloon launch through a thunderstorm cell during the DC-8 flight on May 19. Note the three main charge regions: lower negative charge around 500 mb, middle positive charge near 350 mb, and an upper negative charge just above that. **Fig. S2-B** (right) shows the location of the sounding (blue dot near 36 °**N and -99°E) relative to the thunderstorm cell and the DC-8 flight path. HO_x in pptv are colored along the flight path with the grayscale line underneath representing the presence of flash extent. This sounding appears to have passed near or through the center of convection for this cell, while the DC-8 tended to stay on the outskirts of the cell.**

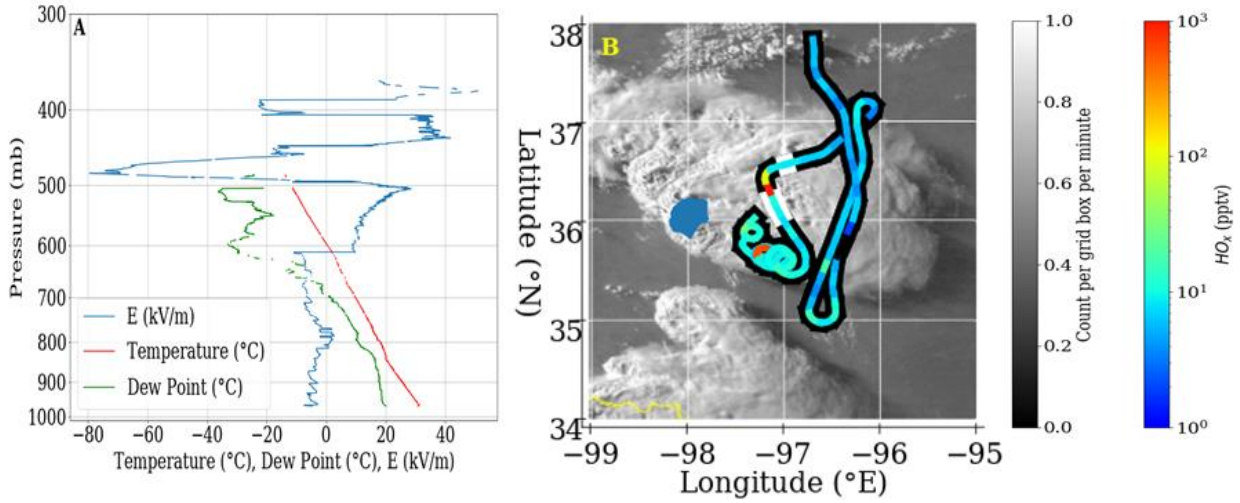

Fig. S4.

Electric field sounding and its corresponding location on May 29. **Fig. 3-A** (left) depicts temperature (red line), dew point (green line) and the local electric field (blue line) recorded during a balloon launch through a thunderstorm cell during the DC-8 flight on May 29. This storm had three main charge regions: lower positive charge from 600-500 mb, middle negative charge just above 500 mb, and an upper positive charge just above that up to about 400 mb. Inverted polarity cells tend to have more positive lightning flashes, which are less likely to be detected by the LMA (*32*). **Fig. 3-B** (right) shows the location of the sounding (blue dot near 36°N and -98°E) **relative to the thunderstorm cell and the flight path of the DC-8. HO_x in pptv are colored along the DC-8 flight path with the grayscale line underneath representing the presence of flash extent. This sounding appears to have been closer to the anvil than the one depicted in Fig. S2 and may be a good indicator of the typical electric field in the anvil nearest this storm core.**

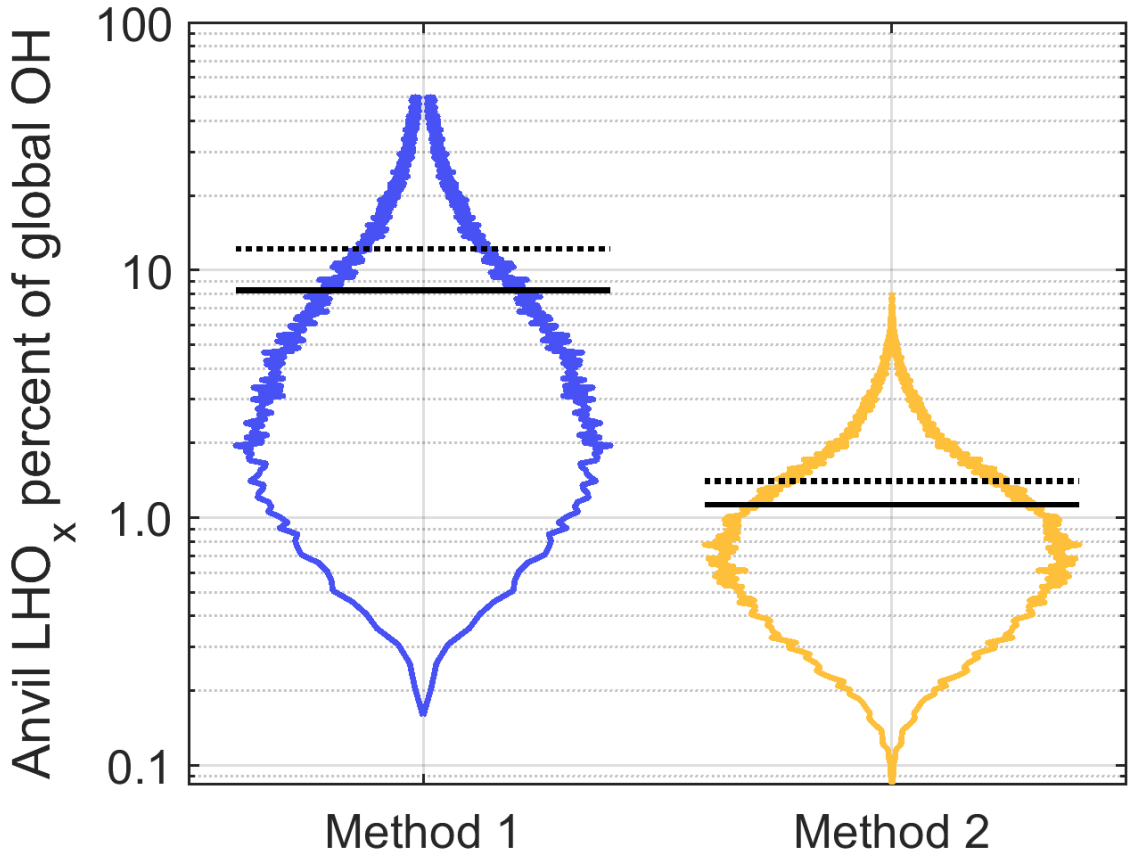

Fig. S5.

Violin plots of the percent that LHO_x contributes to total global OH calculated by the two methods. Histograms with 1000 bins were found for the frequency of LHO_x fraction of the global OH that was calculated by the 100,000 Monte Carlo simulations. They are binned by linear values, but are plotted as mirror images along the y-axis on a logarithm scale to emphasize the lower values. The mean value (dotted line) is greater than the median value (solid line), indicating that the distributions are skewed toward higher values.

Time (UTC)	Anvil Volume (Radar Only) (10^{13} m^3)	Anvil Volume (Radar + Satellite) (10^{13} m^3)	Flash Extent Volume (10^{13} m^3)	% of Anvil with Flash Extent
May 19-20, Oklahoma Region				
00:46:09 – 00:59:01	14.5±2.2	16.6±3.3	0.95	4.8-7.7%
1:02:57 – 1:15:50	14.4±2.2	16.2±3.3	0.97	5.0-8.0%
May 25-26, Oklahoma Region				
1:19:10 – 1:32:20	18.3±2.8	20.2±3.6	3.05	12.8-19.6%
May 29-30, Oklahoma Region				
23:42:43 – 23:54:50	18.8±2.3	20.4±3.3	4.40	18.6-26.7%
00:22:20 – 00:35:38	28.6±3.2	30.9±4.3	3.34	9.5-13.2%
June 22-23, Colorado Region				
00:20:34 – 00:35:29	11.1±1.6	13.6±2.2	2.22	14.0.8-23.3%
00:35:29 – 00:46:04	11.5±1.7	17.0±3.7	3.38	16.3-34.5%
00:51:11 – 1:00:38	12.3±1.9	19.6±3.7	3.06	13.1-29.5%
1:03:27 – 1:12:19	12.9±2.0	21.8±3.7	3.04	11.9-27.9%
1:15:58 – 1:28:57	13.6±2.1	22.0±4.1	3.36	12.9-29.2%

Table S1.
Anvil and LMA region volumes. Volume of the anvil estimated two ways: radar only and radar and satellite. These values were obtained from Pollack et al. (*17*), **Table 3**. Flash Extent volume was calculated from LMA data as the volume that had flash extent values > 0 during the listed time period within the anvil. The percentage of the anvil with flash extent is the quotient of the flash extent volume and anvil volume, with the lower bound representing the flash extent volume divided by the average radar and satellite estimated anvil volume, and the upper bound representing the flash extent volume divided by the average radar only estimated anvil volume. Note that the LMA did not register flashes for a large majority of the anvil.

Day	OH per storm anvil cloud each second (10^{25} molecules s^{-1})		% of Global OH	
	Method 1	Method 2	Method 1	Method 2
29-May	27	1.6	12.1	0.7
22-June	27	3.1	12.2	1.4

Table S2.

Estimated mean number of OH molecules produced per second in the anvil by two different methods, as outlined in the estimation methods and global extrapolation sections above. The percent of global OH was calculated by taking the values obtained by the two methods for the storm anvil cloud, multiplying by the number of active storms at any given time, which is 1800 (*16*), and dividing by the global number of OH molecules existing at each second ($4x10^{30}$ molecules).